Using the numerical simulation and artificial neural network (ANN) to evaluate temperature distribution in pulsed laser welding of different alloys

Muhyaddin J.H. Rawa [a,b], Mohammad Hossein Razavi Dehkordi [c,d], Mohammad Javad Kholoud [c], Nidal H. Abu-Hamdeh [e,f,*], Hamidreza Azimy [c]

[a] *Smart Grids Research Group, Center of Research Excellence in Renewable Energy and Power Systems, King Abdulaziz University, Jeddah, 21589, Saudi Arabia*
[b] *Department of Electrical and Computer Engineering, Faculty of Engineering, K. A. CARE Energy Research and Innovation Center, Jeddah, 21589, Saudi Arabia*
[c] *Department of Mechanical Engineering, Najafabad Branch, Islamic Azad University, Najafabad, Iran*
[d] *Aerospace and Energy Conversion Research Center, Najafabad Branch, Islamic Azad University, Najafabad, Iran*
[e] *Center of Research Excellence in Renewable Energy and Power Systems, Energy Efficiency Group, King Abdulaziz University, Jeddah, Saudi Arabia*
[f] *Department of Mechanical Engineering, Faculty of Engineering, K. A. CARE Energy Research and Innovation Center, King Abdulaziz University, Jeddah, 21589, Saudi Arabia*

ARTICLE INFO

ABSTRACT

The temperature field during laser welding process plays an important role on determining the quality and quantity of the weld bead size, microstructure characterizations and mechanical properties of the welding interface in the thermal engineering applications. In this study, using the numerical simulation, the influence of pulse duration and frequency on the temperature distribution and velocity field in distinctive laser welding of stainless steel 420 (S.S 420)/stainless steel 304 (S.S 304), and Bohler 303 (B 303)/stainless steel 304 (S.S 304) was examined. The results of numerical modeling illustrated that shear stress of Marangoni and buoyancy force are the most curtail aspects in the formation of the flow of liquid metal. A novel artificial intelligence method is proposed to optimally predict the melting ratio, and maximum temperature of the materials. To this end, a combination of ANN and Particle Swarm Optimization (PSO) algorithms are employed. The PSO algorithm is used to optimize the architecture and training algorithm of the ANN, while the ANN is employed for the regression problem. Based on the results, a three-layer feed-forward architecture with sigmoid transfer functions having 17 and 8 neurons in the hidden layers combined with the scaled conjugate gradient backpropagation training scheme is recognized by the PSO as the optimal configuration. Application of optimal ANN to the regression problem results in an acceptable level of error for the training, validation, and test datasets. Finally, the optimized ANN can be utilized to anticipate the melting ratio and thereby the resultant temperature.

1. Introduction

All thermal industries place a great deal of importance on joining and cutting various pieces. Various ways of joining pieces have been put forth over the last few years. The utilization of beams to fuse and cut diverse substances has become a common technique in recent years (Yongbin et al., 2020). Scientists and artisans have given this method some thought because of the considerable heat dissipating ratio in the depth of the item to the width in this sort of welding. This is brought on by the beam's intense focus in the welding zone and its high density. These distinctive qualities have made this approach popular across a range of industries, including construction, automotive, food industries, and biomedical sciences (Yang et al., 2021; Azari et al., 2021). Connecting different alloys to one another is one of the applications for laser welding (Ai et al., 2021). Due to the various qualities of the materials, the application of this technique has been documented in earlier studies (Khan et al., 2021; Algehyne et al., 2021). Elements found in both base metals can be found in the fusion zone. Studying the characteristics and alterations caused by laser parameters is crucial. Numerous numerical techniques have been investigated to assess welding quality. Additionally, the application of numerical simulation techniques improves the welding process' accuracy and quality while lowering manufacturing costs (Peng et al., 2021/05; Grajczak et al., 2021; Zhang et al., 2021; Wang et al., 2021). Due to the special characteristics of these elements,
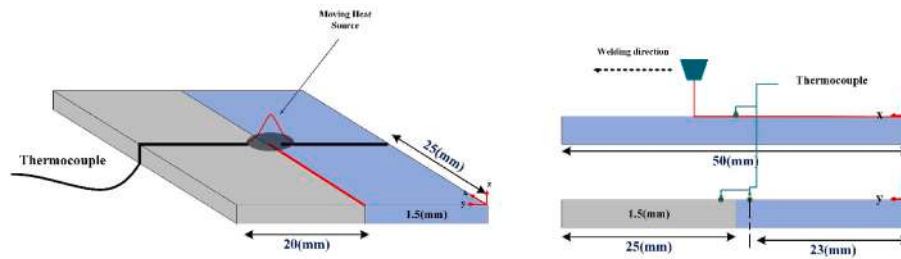

Fig. 1. Laser welding process.

computational modeling of the operation of welding 2 types of steels can result in an optimal weld (Wang and Rong, 2022). Because of their high strength and corrosion resistance, stainless steel alloys require extensive research. Because of this, if a perfect weld is made, it can be used to create tools and equipment for the manufacturing of industrial and medical products.

During laser welding of the brass and stainless steel alloys, Ding et al. (2021) looked at how process variables affected the form of the joint and the temperature distribution. Their findings demonstrated that the liquid metal is asymmetric, which is caused by the brass alloy's lower melting point, which gradually raises the molten pool volume of this alloy. Lin et al.'s (Lin et al., 2021) numerical analysis examined the temperature distribution change and size of the molten pool during the welding of two distinctive metals, AISI 304 and Cu. Their findings demonstrated that the molten pool's and heat field's shapes were asymmetric and diverged in the direction of the AISI 304 sheet. They also demonstrated that the main determinant of the molten pool's size is the laser's power. Dong et al. (2021) looked at how laser welding of two alloys, S.S. 308 and brass, affected the temperature distribution and melting ratio. Their findings demonstrated that utilizing this numerical approach can lower mistake, expense, and time. Yu et al. (2021) looked at the welding characteristics in a laser welding procedure between SS308 and brass. Their findings demonstrated that an asymmetric melting pool had formed, in which the melting of brass had a greater share, due to the low melting temperature and increased thermal conductivity of brass. Li et al.'s (Li et al., 2021) computational analysis examined the mechanical characteristics and microstructure of two types of metals, steel and brass. Their findings demonstrated the high efficiency of laser energy as a bonding waveform parameter in terms of waveform, wavelength, and amplitude. Additionally, it was discovered that the ideal process mode has weldability among the flyer and the material plate at a flight distance of 0.2 mm. The results of a study by Lu et al. (2021) revealed that the dimensions of waveform in the junction zone rise with enhancing laser intensity and along the direction of welding. This was demonstrated by the conclusion of their smooth particle hydrodynamics (SPH) modeling. Normal stress, jet speed, and horizontal welding speed were all related to this discovery. Utilizing the central composite design numerical approach, Saha et al. (Saha and Waghmare, 2020) adjusted the laser welding settings for the S.S. 316. Their findings supported the notion that the quality of the weld is significantly influenced by the laser power, welding speed, and focal distance. Nguyen et al. (2020) looked studied the fusion zone's temperature field and microstructure while using a laser to weld an austenitic stainless steel alloy to copper. Their findings demonstrated that raising the welding speed considerably lowers cracks in the welding zone and lowers the temperature. Due to the greater temperatures for the copper and steel, it was also discovered that raising the laser's power causes the cracks in the fusion area to move to the steel base. Applying Taguchi-based GRA computational modeling, Prabakaran et al. (Prabakaran and Kannan, 2019) improved the procedure variables in the AISI 1018 and AISI 316 process of welding. Their findings demonstrated that the factors of welding speed, laser power, and focal length are useful in assessing the weld quality. They used this technique to demonstrate

that the greatest tensile strength is achieved when welding is done both after heat treatment and after welding. Bhatt et al.'s (Bhatt and Goyal, 2018) investigation looked at how process variables affected the effectiveness of laser welding between brass and S.S 316. Outcomes indicated that when energy increased, each metal's penetration depth also increased, with brass alloys having the greatest rise. Huang et al.'s (Huang et al., 2018) numerical analysis investigated the laser beam welding quality of steel and aluminum alloys. Their findings supported the notion that a keyhole might become more porous and unstable by enhancing the fluid flow behind it.

In a study conducted by Kumar et al. (2017), an examination was undertaken to assess the impact of the laser beam's angle of incidence on the welding procedure of austenitic stainless steel. The findings of their investigation unveiled that diminishing the angle of influence led to a noteworthy alteration in the configuration of the molten pool at an elevated position. The overall geometric shape of the molten pool is associate on the deflection in the angle of influence. The influence of laser welding variables on the welding modality of stainless steel and copper was studied by Chen et al. (2015). Their findings demonstrated that the size of the HAZ is significantly influenced by the laser's characteristics. It was also discovered that joint hardness is decreased by copper melting. Li et al. (2014a) looked at the joint quality between S.S. 316L and H62 brass alloys. Their findings illustrated that the brass overlap structure on the steel improved the performance of the welded joints and prevented the presence of intermetallic composition within the joint. The impact of the beam's intensity on dissimilar laser welding of stainless steel and brass was studied in a different investigation by Li et al. (2014b). Their findings showed that the weld formed had more proper microstructure and mechanical qualities when the power was lower than 1846 W. Sasaki et al. (Sasaki and Ikeno, 2011) looked at the joining performance of steel and brass during a welding of beam laser technique. Their findings shown that a high-quality weld could be obtained by moving the laser's point of emission to brass. Dong et al.'s (Dong and Xiao, 2009) investigation of the effectiveness of laser welding on brass and copper. The outcomes demonstrated that this technique can be used to produce a penetration weld of a satisfactory quality. Additionally, it was discovered that using the best process variables can result in a weld of the appropriate quality. Galun et al.'s (Galun et al., 2002) investigation into the laser welding technique' ability to weld stainless steel and brass alloys. The findings demonstrated that the steel-brass weld strength is superior to the brass-brass weld strength. It was also discovered that using this technique produced welds that were sturdy enough to resist the tensile process. With a pulsed Nd: YAG laser, Geng et al. (2019) performed distinct laser beam welding of S.S. 420 and S.S. 304 to determine the mechanical characteristics, microstructure, and temperature distribution of the welded zone. Investigations were done into how pulse width and frequency affected the temperature change in the fusion zone. According to their findings, the heating and cooling cycles had essentially identical variations caused by the laser pulse time and frequency.

The bulk of previous studies has been focused on one method either numerical simulation or ANN. At this study pulsed laser welding has been modeled through numerical simulation. Many boundary
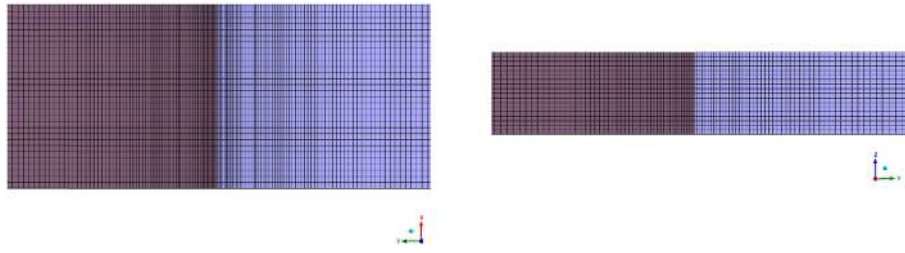
Fig. 2. Grid elements.

Table 1
Elements ratio in 304 and 420 stainless steel (Casalino et al., 2018; Baghjari, 2013).

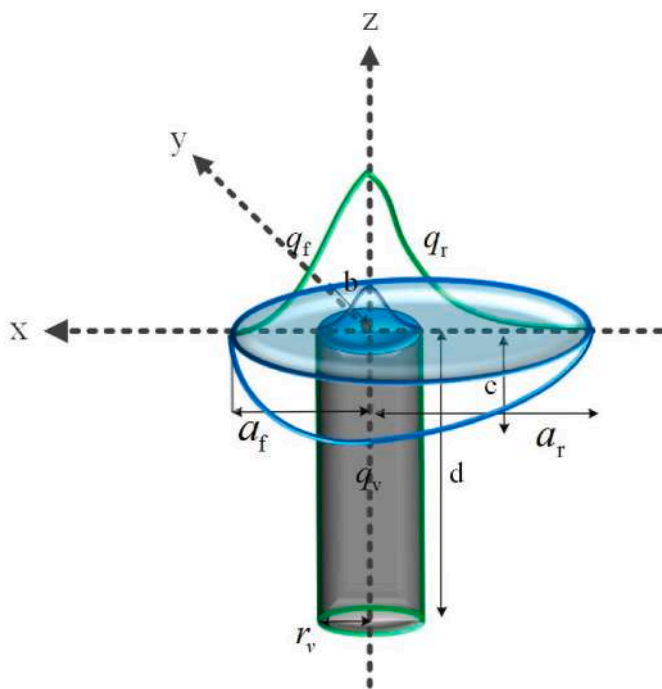| Arrangement		C%	Cr%	Mn%	P%	Si%	Ni%	Fe%
Weight	S.S 304	0.08	18.4	1.06	0.03	0.34	8.9	Balanced
	S.S 420	0.15	13	0.17	0.04	0.46	0.13	Balanced

Fig. 3. Thermal model.

conditions and laser beam at pulse mode have been considered to improve the numerical model accuracy. On the other hand, above ANN modeling based on PSO optimization algorithm was selected to predict the temperature and melt pool dimension. Additionally, there are few studies that investigated both temperature and melt pool geometry at different materials set.

The regressors are the welding speed, frequency, pulse duration, current, and nozzle distance. The regressands were selected the melting ratio, and maximum temperature. This approach was selected for another set laser welding experiment (S.S 304 and bohler 303 steel) with different materials properties to assess the validity of optimized ANN approach.

2. Numerical simulation

The correlation between the temperature differential and the flow of molten metal in the liquid zone substantially impacts the welded alloy's quality and mechanical characteristics. Consequently, correctly

forecasting all aspects that impact temperature and molten flow can enhance welding quality while saving money. In order to carry out numerical simulations of laser welding, a transient modeling based on the finite volume approach was implemented. The thermal energy model and thermophysical parameters were created using a numerical code that incorporated temperature changes into account. Fig. 1 depicts the sheets dimensions as well as an illustration depiction of the laser welding. The temperature history was extracted to investigate diverse factors of laser welding and validate the findings, as depicted in Fig. 1.

One of the fundamental challenges in solving equations involving partial derivatives lies in establishing a suitable grid. Creating an appropriate grid plays a crucial role in simplifying the solution of a set of differential equations. Conversely, an inadequate grid setup can lead to instability or convergence failure in computations. Given that most gradients occur near the laser beam due to the boundary layer, it is possible to effectively represent these variations by increasing the density of mesh points in these regions. The critical consideration is to determine an optimal number of mesh elements.

It should be noted that reducing the size of elements and increasing their quantity will result in a prolonged solution process. Conversely, employing more prominent mesh elements diminishes the accuracy of calculations and the ability to observe phenomena. As depicted in Fig. 2, the quantity of structure grid cells derived from the grid analysis amounted to about 600,000. Table 1 outlines the element structure of stainless steel 304 and 420.

2.1. Modeling the laser welding process

During the keyhole laser welding process, creating a plasma cloud on the surface sheet of the molten pool prohibits the laser beam's distribution energy from accomplishing the keyhole. As an outcome, a certain amount of the heat input is absorbed by the workpiece's surface, known as the inverse absorption phenomenon. The keyhole wall absorbs the remaining radiation by Fresnel absorption (Ducharme et al., 1994). Gaussian elliptic and cylindrical heat flux were used to convey the distribution of absorbed thermal energy at various places throughout the workpiece. The thermal model, as shown in Fig. 3, demonstrates the setup used. Eqs. (1)–(3) (Ai et al., 2017; Xia et al., 2014) include the equations regulating these elliptic and cylindrical heat sources.

$$q_v(x, y, z) = \frac{6f_1\eta p}{\pi r_v^2 d(1 - \exp(-3))} \exp\left(-3\frac{(x^2 + y^2)}{r_v^2}\right)\left(\frac{mz + r_v}{md + 2r_v}\right) \tag{1}$$

$$q_f(x, y, z) = \frac{6\sqrt{3}f_2 f_f \eta p}{a_f bc\pi\sqrt{\pi}} \exp\left(-3\left(\frac{x^2}{a_f^2} + \frac{y^2}{b^2} + \frac{z^2}{c^2}\right)\right) \tag{2}$$

Table 2

Thermophysical characteristics (Zhang et al., 2016; Mills, 2002; Pehlke et al., 1982; Grimvall, 1999).

Nomenclature	Symbol	Material	Value		Unit
Solid phase density	ρ_s	S.S 304	$\rho_s = 8020 - 0.501(T - 298)$		kg m^{-3}
		S.S 420	7860		
Liquid phase density	ρ_l	S.S 304	$\rho_l = 6900 - 0.8(T - 1727)$		kg m^{-3}
		S.S 420	7000		
Solidus temperature	T_s	S.S 304	1673		k
		S.S 420	1727		
Liquidus temperature	T_l	S.S 304	1727		k
		S.S 420	1783		
Temperature in the surrounding environment	T_∞		298		k
Thermal conductivity	k	S.S 304	$k = 10.33 + 15.4 \times 10^{-3}T - 7 \times 10^{-7}T^2$	$298 \leq T \leq 1633$	W m^{-1}k^{-1}
			$k = 355.93 - 196.8 \times 10^{-3}T$	$1644 \leq T \leq 1672$	
			$k = 6.6 + 12.14 \times 10^{-3}T$	$T > 1793$	
		S.S 420	$k = 20 + 61.5 \times 10^{-4}T$	$T < 1727$	
			$k = 133.4 - 594.9 \times 10^{-4}T$	$1727 \leq T \leq 1783$	
			$k = 6.5 + 116.8 \times 10^{-4}T$	$T > 1783$	
Specific heat capacity	c	S.S 304	$c = 0.443 + 2 \times 10^{-4}T - 8 \times 10^{-10}T^2$	$298 \leq T \leq 1727$	J g^{-1}k^{-1}
		S.S 420	$c = 1.92 - 1.587 \times 10^{-2}T - 2$	$1150 \leq T \leq 1173$	
			0.569	$T > 1173$	
Latent heat	L_m	S.S 304	2.90×10^5		J kg^{-1}
		S.S 420	3.04×10^5		
Stefan-Boltzmann coefficient	σ		5.67×10^{-8}		W m^{-2}k^{-4}
viscosity	μ		0.0007		kg m^{-1}s^{-1}

$$q_r(x,y,z) = \frac{6\sqrt{3}f_2 f_r \eta p}{a_r bc\pi\sqrt{\pi}} exp\left(-3\left(\frac{x^2}{a_r^2} + \frac{y^2}{b^2} + \frac{z^2}{c^2}\right)\right) \qquad (3)$$

In the above equations, q_v, q_r, q_f are heat sources, p is the laser energy, f_r, f_f are heat flux coefficients in the fore and rear of the laser beam, f_1, f_2 are the beam energy factors, and a_f, a_r, b, c, d are thermal model coefficients which is depicted in Fig. 3.

2.2. Governing equations

The fluidic motion of molten metal within the pool generates convective heat transfer in laser welding models. As an outcome, the momentum and energy equations must be included in the laser welding model. The liquid fraction is calculated using the following equation to find the areas filled by molten and solid materials. During the freezing or melting of the substance, the liquid fraction takes on values ranging from 0 to 1. The force resulting from the material's phase change can be adequately evaluated by incorporating the liquid fraction into the momentum equation.

$$f_L = \begin{cases} 0 & T \leq T_s \\ \dfrac{T - T_s}{T_l - T_s} & T_s < T < T_l \\ 1 & T \geq T_l \end{cases} \qquad (4)$$

The equations were discretized by incorporating several assumptions. It was assumed that the fluid flow was incompressible, according to the fundamental laws of Newtonian physics, and exhibiting a laminar feature. Furthermore, the impact of liquid metal evaporation was considered negligible. Finally, the study began at a temperature of 25 °C to serve as a reference point. These assumptions were the foundation for discretizing the equations and making following computing techniques easier.

Continuity equation:

$$\frac{\partial \rho}{\partial t} + \nabla \cdot \left(\rho \overrightarrow{U}\right) = 0 \qquad (5)$$

Momentum equation:

$$\frac{\partial\left(\rho \overrightarrow{U}\right)}{\partial t} + \nabla \cdot \left(\rho \overrightarrow{U}\,\overrightarrow{U}\right) = -\nabla p + \nabla \cdot \left(\mu \nabla \overrightarrow{U}\right) + \rho \overrightarrow{g} - \frac{\mu}{K}\left(\overrightarrow{U}\right) \qquad (6)$$

Energy equation:

$$\frac{\partial(\rho H)}{\partial t} + \nabla \cdot \left(\rho \overrightarrow{U}H\right) = \nabla \cdot (k\nabla T) + q \qquad (7)$$

The variables $\rho, H, t, p, \overrightarrow{U}, k, \overrightarrow{g}, K$ and μ represent quantities such as density, enthalpy, time, pressure, velocity, thermal conductivity coefficient, acceleration, coefficient of Darcy resistance and viscosity, respectively.

2.3. Boundary conditions

The surface boundary condition:

$$k\frac{\partial T}{\partial \overrightarrow{n}} = -\varepsilon\sigma\left(T^4 - T_\infty^4\right) - h(T - T_\infty) + q_s \qquad (8)$$

Where ε is the coefficient of emission, σ is the coefficient of Stefan–Boltzmann, T_∞ is the temperatures in the vicinity, and h is the coefficient of convection.

Shear stress:

$$\mu\frac{\partial u}{\partial z} = -\frac{\partial \gamma}{\partial T}\frac{\partial T}{\partial x} \qquad (9)$$

$$\mu\frac{\partial v}{\partial z} = -\frac{\partial \gamma}{\partial T}\frac{\partial T}{\partial y} \qquad (10)$$

The stipulation concerning the lower and lateral surfaces was posited as follows, defining the boundary condition:

$$k\frac{\partial T}{\partial \overrightarrow{n}} = -\varepsilon\sigma\left(T^4 - T_\infty^4\right) - h(T - T_\infty) \qquad (11)$$

2.4. Thermophysical characteristics

Welding demonstrates a considerable parameter variation in direct correlation with temperature. As such, to achieve accurate simulation of pulsed laser welding, it becomes imperative to delineate specific thermophysical properties relative to temperature. Table 2 showcases the comprehensive thermophysical characteristics associated with stainless steel 304 and stainless steel 420 in this context.

3. Laser welding experiments

Dissimilar welding with 750W Nd:YAG laser were conducted on

Table 3

Elements ratio in 304 stainless steel and Bohler 303 (Casalino et al., 2018; Baghjari, 2013; https://www.bohlersteels.co.uk).

Arrangement		C%	Cr%	Mn%	P%	Si%	Ni%	Fe%
Weight	S.S 304	0.08	18.4	1.06	0.03	0.34	8.9	Balanced
	Bohler 303	0.27	14.5	0.65	–	0.3	0.85	–

Table 4

Experimental laser welding conditions.

Test Number	Welding Speed (mm/ min)	Frequency (HZ)	Pulse duration (ms)	Current (A)	Nozzle Distance (mm)	Melting Ratio (bohler 303/S.S 304)	Max. Temperature (°C)	
							Bohler 303	S.S 304
1	350	12	8	120	1	0.48	211	191
2	400	15	8	130	2	0.58	228	198
3	350	12	8	120	3	0.82	218	186
4	400	15	8	130	4	0.68	239	186
5	300	10	6	120	2	0.76	212	163
6	350	12	8	120	3	0.71	215	166
7	250	10	8	100	3	0.78	205	146
8	400	15	8	130	4	0.58	224	195
9	300	10	6	120	2	0.61	204	181
10	300	10	6	120	4	0.78	185	125
11	450	20	8	130	3	0.78	205	145
12	400	15	8	130	2	0.9	190	143
13	350	12	8	120	5	0.83	159	119
14	350	12	8	120	3	0.7	155	114
15	350	12	8	120	3	0.73	230	181
16	350	12	8	120	3	0.80	228	172
17	300	10	6	120	4	0.85	195	152
18	500	20	12	130	1	0.92	248	198
19	500	20	12	130	1	0.81	226	173
20	450	20	8	130	4	0.64	182	148
21	250	10	8	100	2	0.51	196	126

Table 5

Laser welding parameters to investigate the impact of pulse duration.

Case	Speed (mm/s)	Pulse duration (ms)	Frequency (Hz)	Laser energy (A)	Focal position (mm)
1	3.1	8	15	130	0
2	3.1	12	15	130	0

different base materials configuration including bohler 303 steel with austenitic stainless steel 304. The samples were selected with dimensions (50 × 25 × 1.5 mm). The chemical composition of materials is presented in Table 3. The raytools laser welding head BW210 with Co-axial nozzle blowing argon gas for protecting melt pool region was utilized.

A CNC table with three-axis (2 axis interpolates) was used for the laser beam motion. For measurement of melt pool depth and width, the welded samples were prepared under ASTM E3 for metallography tests. The optical microscope, model GX53 was used for measuring dimensions of melt pool. Two K-type thermocouples with 1 mm tip diameter were utilized for temperature measurement through Advantech USB-4718. The experimental tests results presented in Table 4.

4. Results and discussions

When various input elements are considered, a precise assessment of temperature, velocity field, and the weld bead size may greatly impact weld quality. To obtain the necessary molten pool qualities in dissimilar material welding, the appropriate range of laser parameters must be determined while considering the specific thermal properties of alloys. As a result, this section dives into how the factors of laser welding affect the distribution of temperature and velocity, as well as the size of the weld bead. The ability to predict temperature dispersion allows for the

modulation of fundamental microstructural features. As a result, several pulse lengths and frequencies were used to create a comprehensive temperature record.

4.1. Impact of pulse duration on temperature field

The temporal extent of the pulse duration exerts a profound influence on the weld's overall quality. Through judicious manipulation of the pulse duration, one can effectively avert the emergence of fractures brought about by expeditious solidification. A comprehensive analysis of the pulse width's repercussions is expounded upon in Table 5, delineating the pertinent parameters for scrutiny.

An examination was conducted to evaluate the impact of variations in pulse duration on the temperature distribution. The investigation focused on analyzing the temporal temperature profile at various distances perpendicular to the workpiece's edge, particularly at a location 25 mm away. Fig. 4 depicts this analysis. Upon careful examination of Fig. 4, it becomes apparent that a decrease in pulse width results in decline temperatures at different intervals while the pattern of temperature oscillation remains unaffected. This is evident from the significant rise down of approximately 490 °C in the maximum temperature at the junction of the two parts. However, a more detailed examination of the figure reveals that as the pulse width increases, the slope of temperature changes at a distance of 1 mm from the line of welding also increases. The dissimilarity in the thermal conductivity coefficients of stainless steel 304 and 420 accounts for the temperature disparity between them. The lower thermal conductivity coefficient of stainless steel 304, compared to stainless steel 420, restricts thermal penetration into stainless steel 304, resulting in higher temperatures near the laser beam than stainless steel 420.

Nevertheless, it is essential to note that when the beam of laser has not yet surpassed the 25 mm mark from the workpiece's edge, the temperature of stainless steel 420 exceeds that of stainless steel 304 due
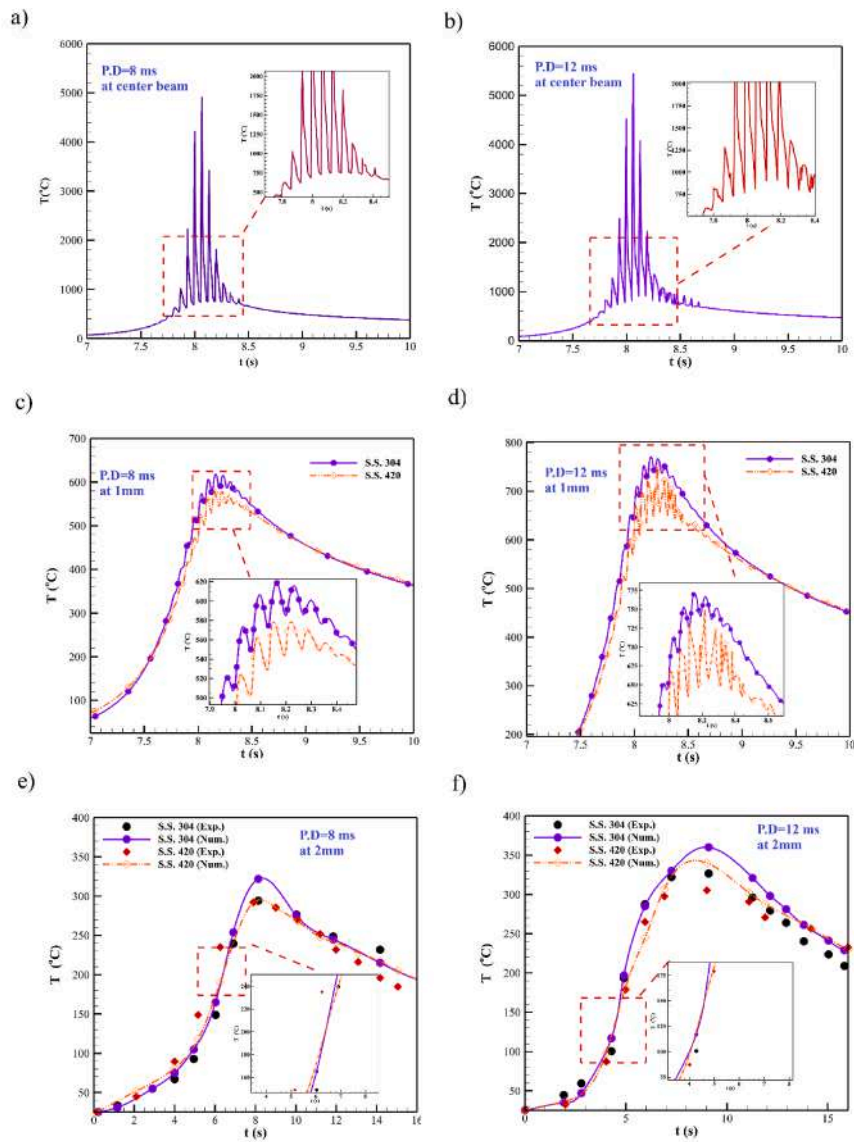
Fig. 4. Temperature changes as a function of time at pulse duration of 8 and 12 ms.
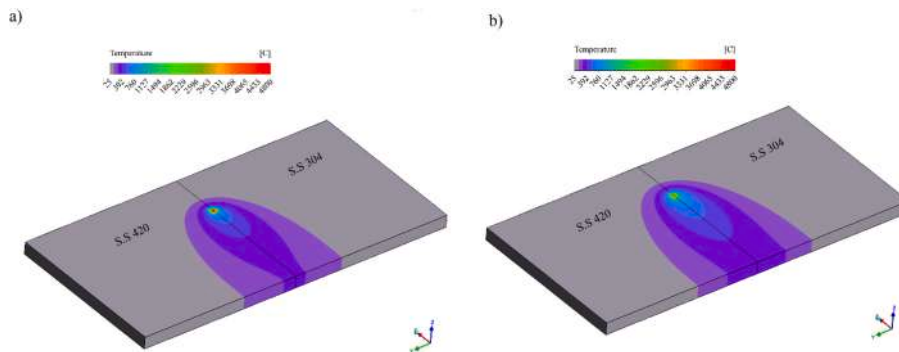

Fig. 5. Contour of temperature at pulse duration of a) 8ms and b) 12ms.

to the small thermal diffusivity of stainless steel 420 at lower temperatures. Fig. 4e and 4f compare the temperature profiles acquired from numerical modeling and the experimental investigation conducted by Geng et al. (2019), Specifically, at an acquired interval of 2 mm from the laser beam's capital. The results from the numerical simulations align well with the experimental data, thus validating the accurate

characterization of properties and the thermal model.

The contour diagram in Fig. 5 depicts the thermal distribution at workpiece's perimeter at the extremity of the pulse duration. It is clear that when the pulse duration decline, decreasing the pulse energy, the temperature at the nucleus of the molten pool rises down by around 245 °C. Also, with the decrease in pulse duration, it is observed that the

Table 6
Laser welding parameters to investigate the impact of frequency.

Case	Speed $\left(\frac{mm}{s}\right)$	Pulse duration (ms)	Frequency (Hz)	Laser energy (A)	Focal position (mm)
3	6.2	9	15	130	0
4	6.2	9	20	130	0

area affected by heat has declined significantly.

4.2. Impact of frequency on temperature field

Table 6 presents the data Designed to examination the impact of frequency on the field of temperature, velocity, and size of the weld bead. By skillfully using the frequency during laser welding, one can proficiently control the energy input to the sheet and the thermal cycle. Therefore, this section investigated the influence of frequency on temperature and velocity field.

Fig. 6 illustrates the temporal temperature profiles corresponding to 15 Hz and 20 Hz frequencies. The obtained data unveils that decreased frequency leads to decline temperatures at varying positions. Moreover, lower frequencies give rise to reduced temperature fluctuations across different time intervals. The figure shows that the molten pool reaches its highest temperature at about 4500 and 5150 °C for 15 and 20 frequencies, respectively. As the distance from the central beam expands, the maximum temperature is observed later due to heat diffusion in the surrounding region. At a frequency of 15 Hz, an approximate temperature difference of 60 °C exists between stainless steel 304 and 420 situated 1 mm away from the workpiece joint. In contrast, at a higher frequency, this disparity amounts to 75 °C. Fig. 7 displays the temperature field of the sheet for frequencies of 15 Hz and 20 Hz. The distribution of temperatures is skewed towards stainless steel 420 due to its high thermal diffusivity.

4.3. Impact of pulse duration on velocity field

Because of surface tension, the molten pool generates liquid metal flow. This flow is caused by the force of surface tension, which fluctuates
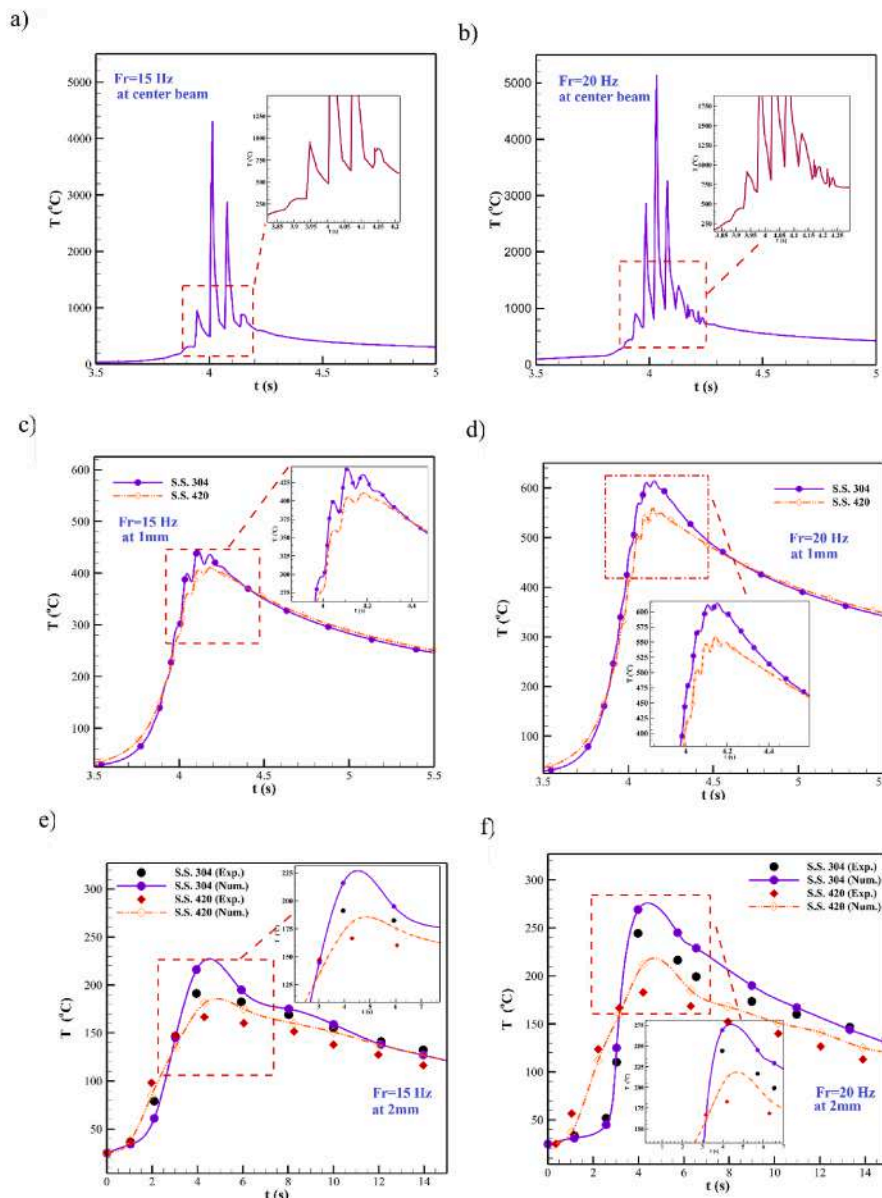

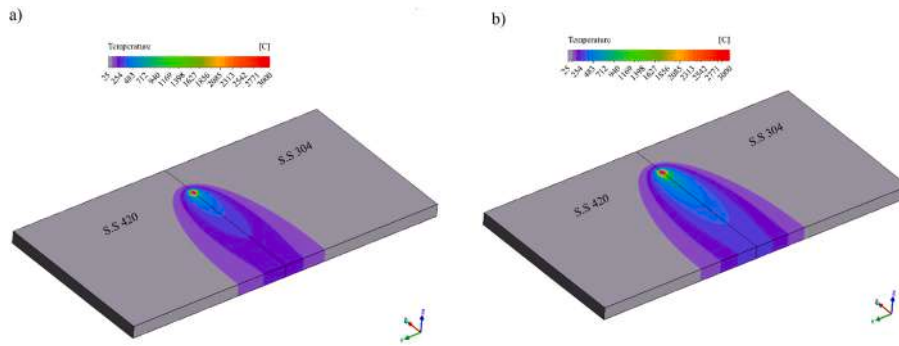**Fig. 6.** Temperature changes as a function of time at frequency of 15 and 20 Hz.

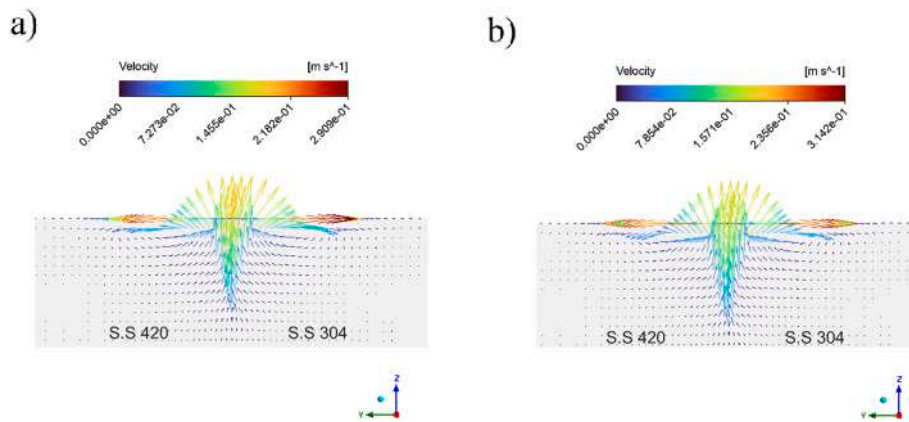**Fig. 7.** Contour of temperature at frequency of a) 15 Hz and b) 20 Hz.

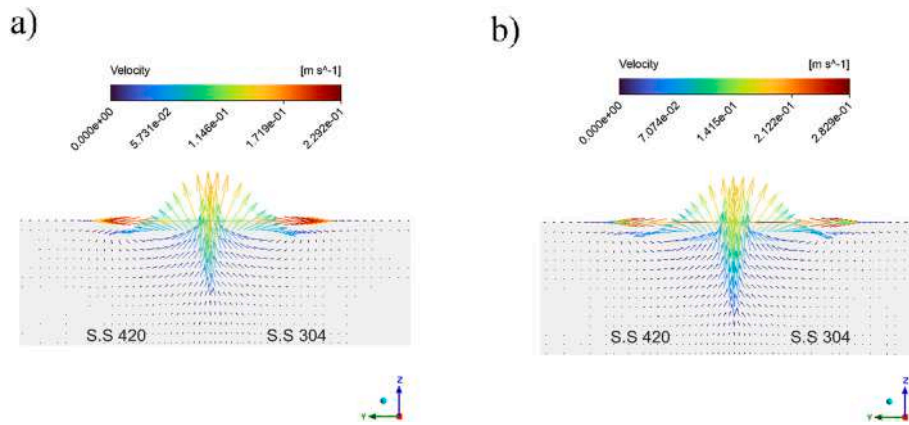**Fig. 8.** Velocity vector at pulse duration of a) 8ms and b) 12ms.

Fig. 9. Velocity vector at frequency of a) 15 Hz and b) 20 Hz.

in reaction to temperature variations. As a result, temperature oscillations appear on the molten pool's surface. These temperature changes cause an imbalance in surface tension along the workpiece, forming Marangoni flow within the molten area. With a negative Marangoni coefficient, the surface tension decreases as temperature rises, forcing the melt to transfer from the hot area to the mushy region.

The phenomenon of surface tension decreases as temperature increases on account of the intrinsic surface-active components in steel. Fig. 8 depicts the vector pattern found at the cross-sectional junction of the sheet at different pulse durations. Significantly, a conspicuous diversion of the molten metal flow towards the sheet possessing a substantially higher temperature gradient becomes apparent due to the pronounced discrepancy in temperature gradients between stainless

steel 304 and 420. Fig. 9 shows the vector pattern found at the cross-sectional junction of the sheet at different pulse frequencies. The depicted illustration demonstrates that alterations in the temporal dynamics of the pulse yielded negligible implications on the trajectory of melt motion, solely resulting in variations in velocity.

4.4. Impact of frequency on velocity field

As the temperature increases, the presence of surfactant elements within stainless steel leads to a reduction in surface tension. An elevation in the shear stress exerted on the sheet's surface as a consequence of the gradient in surface tension prompts an augmentation in the breadth of the liquefied reservoir. The 9th figure elucidates the vector of velocity. It
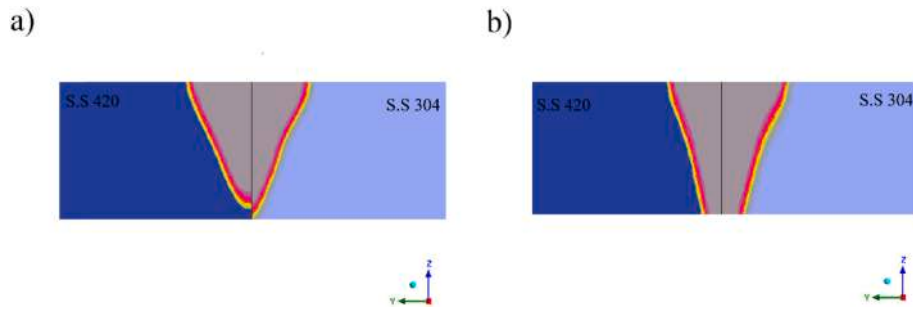
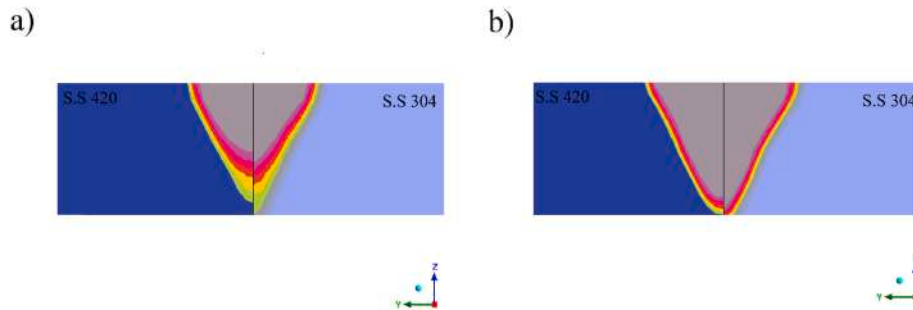**Fig. 10.** Molten pool at pulse duration of a) 8 ms and b) 12ms.

Fig. 11. Molten pool at frequency of a) 15 Hz and b) 20 Hz.

is discernible that as the frequency amplifies because of the augmentation in the temperature differential, the velocity of the molten metal escalates. By increasing the frequency by 5 Hz, the melt flow velocity has increased by 23%. Consequently, this engenders an upsurge in heat conduct by displacement within the liquefied area and an enlargement in the area affected by thermal influence.

4.5. Impact of pulse duration on molten pool

An accurate estimate and projection of weld bead size under various laser settings might provide helpful information for attaining the required connectivity between the two metallic sheets. This predictive analysis has the potential to improve welding precision and effectiveness.

The enlargement of pulse duration engenders an amplification in both the magnitude of the molten area and the heat-affected region, owing to the protracted transfer of heat. Fig. 10 visually represents the proportion of mass of liquid. The coefficient of thermal conductivity inherent in stainless steel 304 yields insignificant heat dissipation to the adjacent region. Consequently, the weld bead and the heat-affected area dimensions exhibit superior qualities for stainless steel 304 compared to stainless steel 420.

4.6. Impact of frequency on molten pool

The size and arrangement of the liquid pool significantly impact the weld integrity between the two constituents. As mentioned earlier, the disparate thermal characteristics of the workpieces result in an uneven temperature dispersion both on the surface and within the internal sections of the workpieces. Accordingly, as illustrated in Fig. 11, the liquefied pool manifests an asymmetrical form when observed in a cross-sectional view. It is worth noting that by lowering the frequency, the duration required for the absorption of thermal energy decreases, leading to inadequate penetration of the molten flow into the deeper regions of the workpiece.

5. The artificial intelligence approach to detect the optimal ANN configuration

Artificial Neural Networks (ANNs) are appropriate for regression problems due to their ability to approximate non-linear functions, adaptability, generalization to unseen data, representation learning from raw input data, parallel processing, robustness to noise and incomplete data, and support for incremental learning (Alsheikhy, 2022). ANNs can effectively capture complex relationships, handle non-linearity, learn from imperfect data, and adapt to various real-world scenarios, making them highly suitable for function approximation tasks (Chen, 2022; Gaur et al., 2022). The universal approximation theorem states that there are ANNs with a finite number of neurons that can approximate any continuous function to any desired level of accuracy, given the appropriate activation function and a sufficiently number of neurons.

While the universal estimation theorem assurance the existence of an ANN that can approximate the considered function to any desired level of accuracy, it does not specify a particular ANN architecture or learning algorithm. The main reason is due to varying problem complexities, input data characteristics, target variable properties, available data sizes, and performance trade-offs. Therefore, each regression problem requires a tailored approach considering several factors. Customizing the ANN's architecture and training algorithm based on these factors ensures accurate function approximation and optimal performance for each specific regression task.

The following properties can be considered for ANNs used for the regression problems (Hanif et al., 2022; Liu and Lu, 2022).

- Feed-Forward (FF) and Cascade-Forward (CF) networks are two common types of neural network architectures used for regression analysis. A Feed-Forward network consists of input, hidden, and output layers, and information flows in a forward direction. It is effective for capturing complex relationships and approximating functions. Cascade-Forward networks, on the other hand, dynamically add neurons during the learning process, allowing the network to adapt and expand its complexity. They employ a cascade

Table 7

The possible configurations for the ANN used for the regression problems.

The design parameter	The configurations
Architecture	Feed-Forward or Cascade-Forward networks
Number of layers	2 or 3
Hidden neuron of any layer	6 to 20
Activation Function	the sigmoid function or the hyperbolic tangent function
Supervised learning method	the Levenberg-Marquardt backpropagation, bayesian regularization backpropagation, or scaled conjugate gradient backpropagation

Table 8

The PSO factors used in this examination.

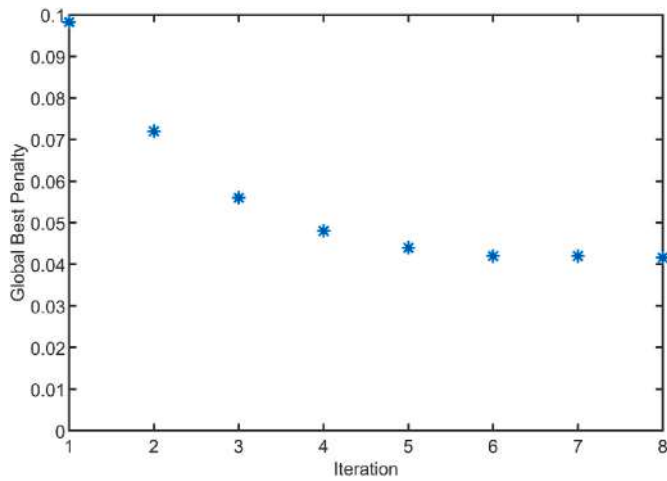| Parameter	Values
Swarm Size N	50
Maximum Iteration	100
acceleration coefficient c_1	1
acceleration coefficient c_2	1
Inertia Weight ω	0.5

Fig. 12. The penalty function evaluated during the optimization process.

Table 9

The optimal ANN configurations found by the PSO.

	Parameter	Values
The ANN configuration	Architecture	Feed-Forward
	Number of layers	3
	Hidden neurons	17, 8
	Activation Function	sigmoid
	Supervised learning method	scaled conjugate gradient backpropagation
The penalty value		0.0416

correlation learning algorithm and automatically determine the network structure. The choice between FF and CF networks depends on factors such as problem complexity and available training data.

- In neural network architectures, there is no restriction on the number of layers that can be used. This means that different structures can have varying numbers of layers, providing flexibility in designing networks. Additionally, within a given network structure, each layer can have a different number of hidden neurons. This allows for customization and adaptability in capturing the complexity and relationships of the data. The ability to have varying numbers of layers and hidden neurons in different layers enables neural networks to
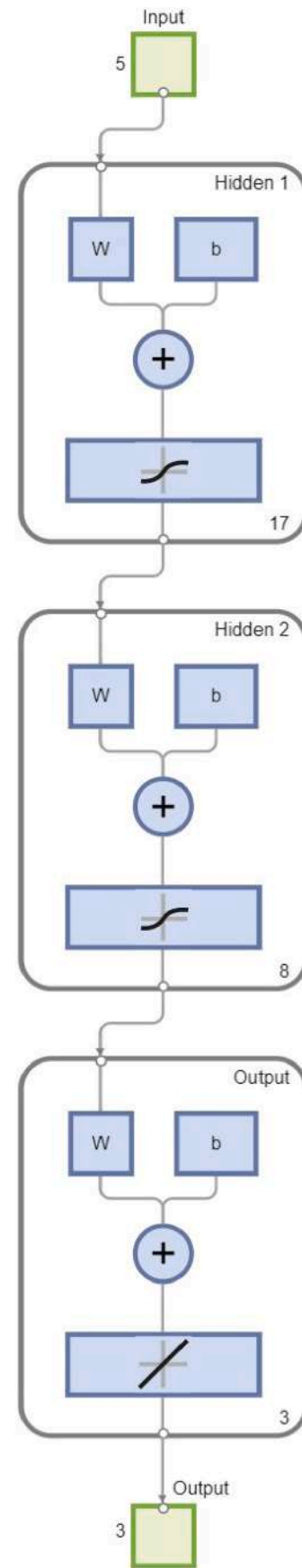

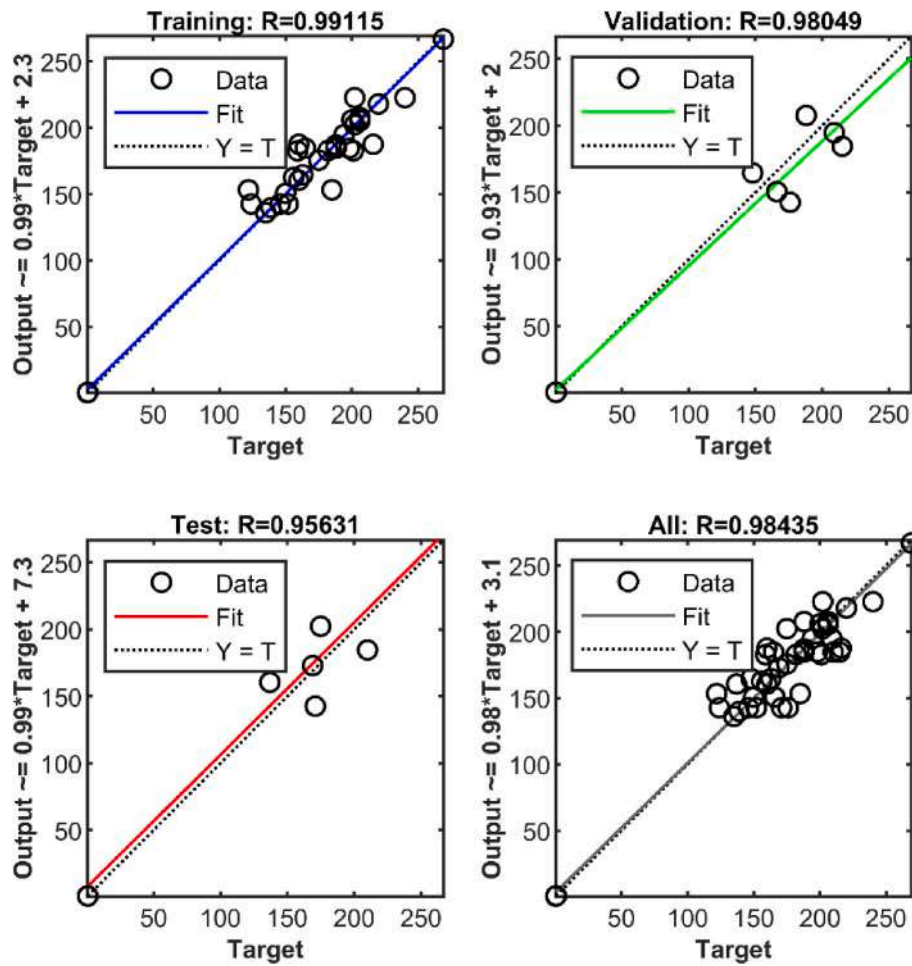**Fig. 13.** The optimal architecture obtained by the PSO.

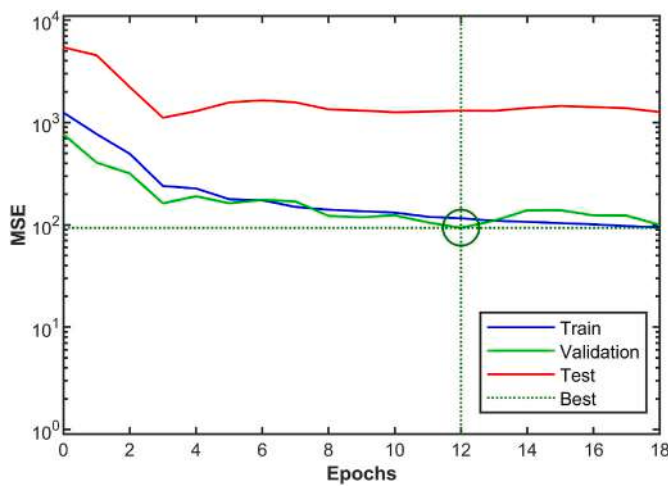**Fig. 14.** The regression diagram for the optimized ANN.

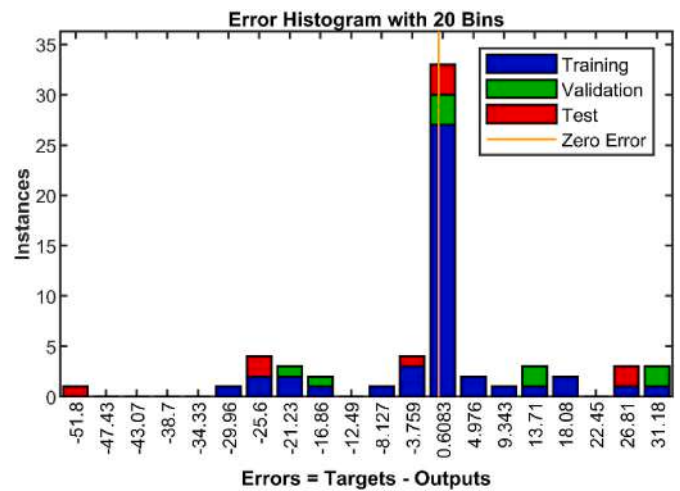**Fig. 15.** The performance diagram for the optimized ANN.

Fig. 16. The error histogram for the optimized ANN.

handle a wide range of problems, accommodate different levels of complexity, and effectively learn from diverse datasets.

- Neural networks offer a variety of activation functions that can be used inside the neurons. Activation functions characterize the output of a neuron based on the weighted sum of its inputs. Different activation functions have distinct properties and impact the network's behavior and learning capabilities. Common activation functions

include the sigmoid function and the hyperbolic tangent function. The choice of activation function depends on the specific problem, the desired behavior of the network, and the characteristics of the data. By selecting an appropriate activation function, neural networks can effectively model non-linear connections and capture convened patterns in the data.
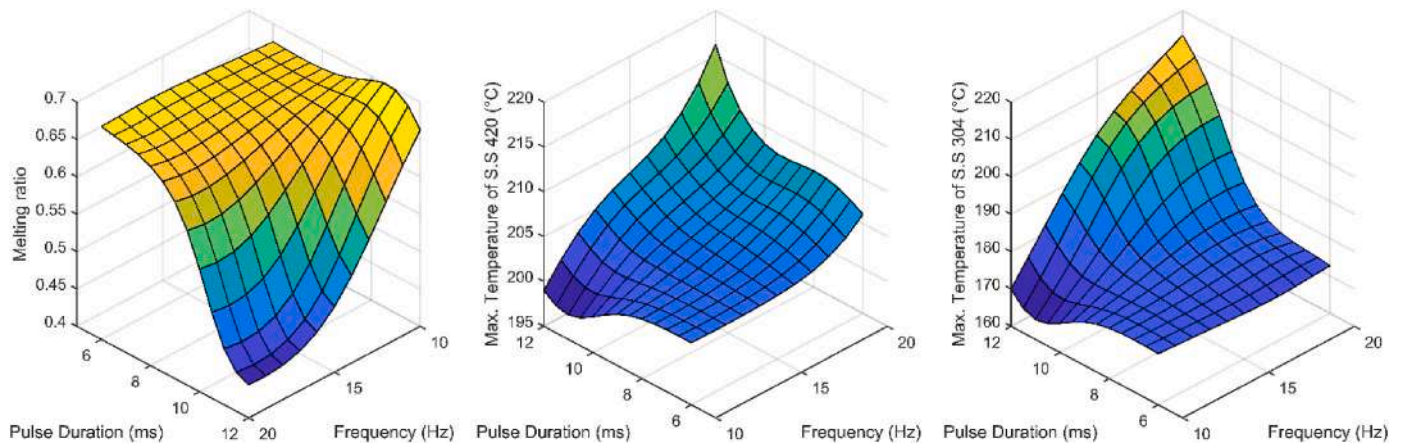
Fig. 17. The influence of the frequency and pulse duration for laser welding of S.S 420/S.S 304.
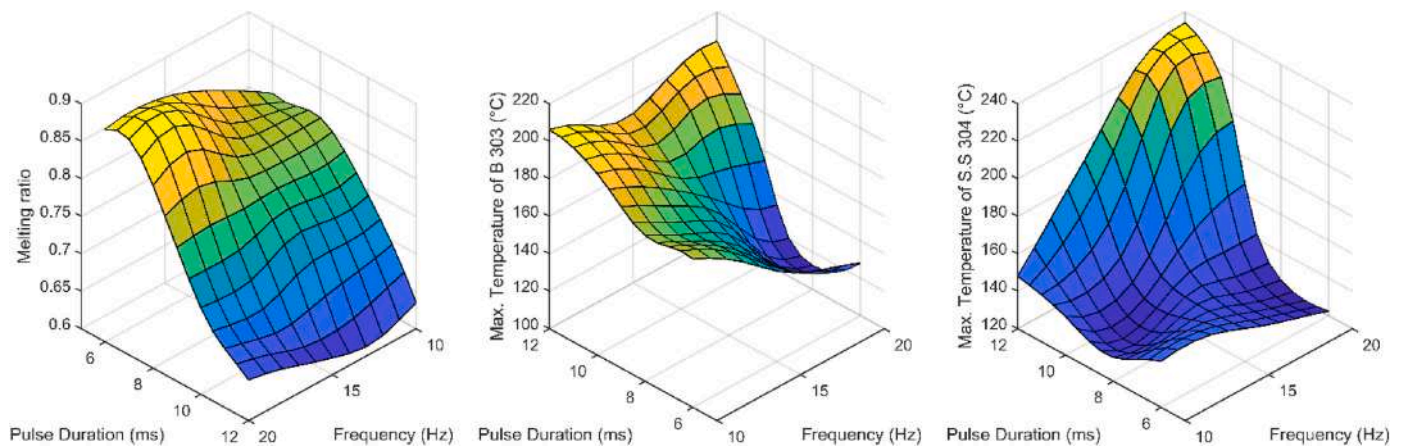

Fig. 18. The influence of the frequency and pulse duration for laser welding of B 303/S.S 304.

- In the field of neural networks, there exists a wide range of training algorithms that are used to adjust the weight and bias matrices within the network. These algorithms aim to optimize the network's performance by minimizing the difference between the predicted outputs and the actual targets during the training process. Some popular training algorithms include the Levenberg-Marquardt backpropagation "trainlm", bayesian regularization backpropagation "trainbr", and scaled conjugate gradient backpropagation "trainscg". The choice of training algorithm depends on factors such as the problem complexity, available training data, computational resources, and desired convergence speed. Each algorithm has its own strengths and limitations, and the selection of the appropriate training algorithm plays a crucial role in achieving optimal performance and accuracy in neural network training.

As can be seen, several ANN configurations can be selected for any regression problem. To select the proper configuration, there may be two general approaches.

- When selecting the properties of an ANN, experts follow a systematic approach. They analyze the problem, determine the network type, select an appropriate activation function, design the architecture with the desired number of layers and neurons, choose a suitable training algorithm based on the problem's characteristics, employ regularization techniques to prevent overfitting, evaluate performance using cross-validation, and iteratively refine the network through experimentation. Expertise in neural networks, data analysis, and domain knowledge is crucial for making informed decisions

and optimizing the network for accurate predictions and desired performance.

- Artificial Intelligence (AI) can assist in selecting the properties of an Artificial Neural Network (ANN) by analyzing data, automating architecture search, optimizing hyperparameters, employing reinforcement learning, automating evaluation and comparison, and integrating expert knowledge. AI techniques provide data-driven insights, automate optimization processes, and enable efficient exploration of the ANN design space. This integration of AI and ANN property selection enhances the effectiveness and efficiency of decision-making, facilitating the design of optimized neural networks for various tasks.

In this paper, the second approach is considered. A novel AI model is proposed to find the optimized architecture and training algorithm of the ANN for the considered regression problem (Ahmad, 2022; Khan et al., 2022; Deng et al., 2022). Table 7 shows the possible choices for the ANN used for the regression problems. As can be seen, there are 2880 possible combinations. Obviously, it is not possible to try all the possible combinations. Therefore, an optimization algorithm is needed to find the best ANN configuration by changing the design parameters.

6. The optimal artificial neural network

6.1. The regression problem

In this study, the laser welding of the following materials is investigated.

- Stainless steel 420 (S.S 420) and stainless steel 304 (S.S 304) (Geng et al., 2019).
- Bohler 303 (B 303) and stainless steel 304 (S.S 304).

The regressors are the welding speed, frequency, pulse duration, current, and nozzle distance. The speed of welding ranges from 250 to 500 mm/s. The frequency of 10–20 Hz is investigated. The pulse duration of 6–12 ms is examined. The current in the interval of 100–130 A is tested. The distance of nozzle of 1–5 mm is studied. The regressands are the melting ratio, and maximum temperature for the materials. There are 21 experiments for any couple of materials with similar regressor combinations.

6.2. The optimization algorithm

In this paper, PSO algorithm is utilized to find the optimal ANN configuration. The PSO algorithm is a population-based optimization technique that simulates the collective behavior of particles in a search space. In PSO, a group of particles represents potential solutions within a search space, with each particle navigating the space by adjusting its position and velocity based on its own experience and the experiences of neighboring particles. By iteratively updating the positions and velocities of the particles, PSO seeks to find the optimal solution by optimizing a fitness function. Through continuous exploration and exploitation of the search space, the PSO efficiently converges towards promising regions, enabling the discovery of optimal or near-optimal solutions.

The algorithm begins by initializing a population of particles, where each particle represents a potential solution to the optimization problem. The particles are assigned random positions and velocities within the search space. During each iteration, known as a "generation", the particles update their positions and velocities based on their own experiences and the information shared by neighboring particles. The position update is influenced by two factors: the particle's own best-known position, called the "personal best", and the best-known position discovered by any particle in the swarm, called the "global best". The velocity update is determined by a weighted combination of the particle's current velocity, its cognitive component, and its social component. These components are controlled by acceleration coefficients, which determine the balance between exploration and exploitation. This algorithm can be represented as follows:

$$v_i^j(t+1) = \omega v_i^j(t) + c_1 r_1(t)\left(pbest_i^j - x_i^j(t)\right) + c_2 r_2(t)\left(gbest^j - x_i^j(t)\right) \quad (12)$$

$$x_i^j(t+1) = x_i^j(t) + v_i^j(t+1) \quad (13)$$

Where $v_i^j(t)$ is the velocity of particle, $x_i^j(t)$ is the current position of particle, $pbest_i^j$ is the personal best position of particle, $gbest^j$ is the global best position, ω is the inertia weight, and c_1 and c_2 are acceleration coefficients.

As the algorithm progresses, particles explore the search space, continuously updating their positions and velocities. The aim is to converge towards the optimal solution by iteratively refining the personal and global best positions. The algorithm terminates either when a predetermined number of generations is reached or when a termination criterion (e.g., a desired fitness level) is met.

In this paper, the penalty function is defined as follows:

$$P = a|A - 1| + b|B| - c(R - 1) \quad (14)$$

Where A, B, and R are the slope, the y-intercept, and the regression value of the regression plot, respectively. The constants a, b, and c are chosen based on the importance of A, B, and R. In this paper, the following values are employed:

$$\begin{aligned} a &= 1 \\ b &= 1e - 3 \\ c &= 1 \end{aligned} \quad (15)$$

The PSO parameters are important because they directly influence the algorithm's performance, balance between exploration and exploitation, problem-specific adaptation, avoidance of premature convergence or stagnation, and computational efficiency. By carefully tuning these parameters, researchers and practitioners can enhance the algorithm's capability to detect optimal or near-optimal solutions, adapt to different problem characteristics, prevent premature convergence, and improve computational efficiency. The PSO parameters used in this study are presented in Table 8.

6.3. Results of Particle Swarm Optimization

The penalty function of Eq. (14) evaluated during the optimization process is depicted in Fig. 12. As can be seen, the global best penalty values are converged after a few iterations of the PSO algorithm. In other words, the particles have recognized the global best position. The optimal solution discovered by the PSO, namely the optimal ANN configuration and the corresponding penalty value is reported in Table 9. Also, the optimal architecture obtained by the PSO is illustrated in Fig. 13.

6.4. Results of the optimal ANN

A regression plot is a visual representation that compares the predicted outputs of the ANN with the actual target values in a scatter plot. The plot helps evaluate the performance of the ANN by examining the relationship between the predicted and target values. Ideally, the data points should align closely along a straight line, indicating a strong correlation. The training plot helps monitor the model's performance on the training data and assess how well it captures the underlying patterns. The validation regression plot, on the other hand, is generated using a separate validation dataset that is not used for training. By analyzing the plot, one can halt the training process to preserve the model generalization, and prevent the over-fitting. The construction of the test regression plot entails utilizing a separate test dataset that remains untapped during the training or validation phase. This approach facilitates a conclusive evaluation of the model's efficacy on entirely novel data, thereby assessing its aptitude to generalize to previously unseen instances. Moreover, it furnishes an unbiased metric to gauge the model's effectiveness objectively. The regression plot for the optimized ANN is shown in Fig. 14. As can be seen, the ANN is almost perfect for the prediction of the outputs.

A performance plot for an ANN summarizes the model's performance during training by evaluating the Mean Squared Error (MSE) for the training iterations (epochs). It includes a training performance curve, showing the model's progress on the training data, and a validation performance curve, indicating its ability to generalize to unseen data. The plot helps identify convergence, overfitting, and informs optimization decisions. The performance for the optimized ANN is illustrated in Fig. 15.

The error histogram for an ANN provides a summary of the distribution of prediction errors made by the model. It visualizes the frequency or count of errors at different magnitudes or ranges. The histogram helps understand the accuracy and precision of the ANN's predictions by examining the distribution of errors. It allows identification of any systematic biases or trends in the errors, such as underestimation or overestimation. By analyzing the error histogram, one can gain insights into the model's performance, assess the overall quality of predictions, and identify areas for improvement. The error histogram for the optimized ANN is illustration in Fig. 16. As can be seen, the error histogram shows that the optimal ANN has an allowable level of error because the majority of errors are concentrated within the central bins.

The error distribution does not exhibit significant biases or outliers that could indicate major flaws in the model's performance.

Ultimately, the enhanced artificial neural network (ANN) possesses the potential to be employed in the estimation of the melting ratio and utmost temperature of the substances. In order to examine the impact of frequency and pulse duration, the other predictors, namely welding speed, current, and nozzle distance, remain unchanged. As illustrated in Figs. 17 and 18, the outcomes pertaining to the laser beam welding process of S.S 420/S.S 304 and B 303/S.S 304 are presented correspondingly.

7. Conclusions

This research examines the impact of laser welding factors on temperature, velocity field, and dimensions in light of the growing demand from industries to conjoin dissimilar alloys. The investigation is conducted utilizing numerical modeling and an ANN model. This study developed a comparison for prediction of melt pool geometry and temperature near the melt pool between numerical simulation results and ANN. The final ANN according to optimization algorithm was selected to model laser welding responses. To ensure precise laser welding modeling, the thermophysical properties are defined as a function of temperature, and a combination of 2 various heat fluxes are employed. The ensuing findings are outlined below.

- Owing to the distinct materials laser beam welding of two sheets, the temperature field exhibits asymmetry, whereby stainless steel 304 undergoes higher temperatures than stainless steel 420, owing to its lower thermal conductivity coefficient.
- The shear stress induced by the surface tension gradient at the molten pool's surface and buoyancy force induces liquid metal flow.
- Reducing the pulse duration from 12 to 8 ms results in an approximate 298 °C increase in the temperature of the molten zone.
- By extending the frequency, the depth of penetration of the molten material into the workpiece is enhanced.
- The optimized ANN regression plot exhibited a robust association between the anticipated and desired values, signifying the model's exceptional skill in prognosticating outputs.
- The optimized artificial neural network (ANN) error distribution revealed that the model's predictions exhibit an acceptable error level. Most errors were concentrated within the zero bins, indicating a lack of notable biases or outliers in the predictions.
- Comparison of both model optimized domain of process parameters implies that optimized welding condition of S.S 304/bohler 303 steel has had wider range of temperature selection to meet the higher welding melt ratio.

For the future work, we aim to couple new numerical simulation methods results by ANN and optimization algorithm to predict the unknown dissimilar laser welding result before welding test.

CRediT authorship contribution statement

Muhyaddin J.H. Rawa: conducted, Methodology, performed the, Resources, performed the, Writing – review & editing, the paper, revised the paper. **Mohammad Hossein Razavi Dehkordi:** conducted, Methodology, conducted the, Investigation, Writing – original draft, revised the paper. **Mohammad Javad Kholoud:** done the, Formal analysis, performed the, Resources, Writing – original draft. **Nidal H. Abu-Hamdeh:** conducted, the, Investigation, performed the, Writing – review & editing, the paper, revised the paper, were, Supervision, of work. **Hamidreza Azimy:** done the, Formal analysis, conducted the, Investigation, performed the, Writing – review & editing, the paper, were, Supervision, of work.

References

Ahmad, F., 2022. Deep image retrieval using artificial neural network interpolation and indexing based on similarity measurement. CAAI Trans. Intell. Technol. 7 (2), 200–218. https://doi.org/10.1049/cit2.12083.

Ai, Y., Jiang, P., Shao, X., Li, P., Wang, C., 2017. A three-dimensional numerical simulation model for weld characteristics analysis in fiber laser keyhole welding. Int. J. Heat Mass Tran. 108, 614–626.

Ai, Y., Liu, X., Huang, Y., Yu, L., 2021. Investigation of dissimilar fiber laser welding of low carbon steel and stainless steel by numerical simulation. J. Laser Appl. 33 (1), 012046, 2021/02/01.

Algehyne, E.A., Saeed, T., Ibrahim, M., Berrouk, A.S., Chu, Y.-M., 2021. Investigation of dissimilar laser welding of stainless steel 304 and copper using the artificial neural network model. J. Laser Appl. 33 (2), 022010.

Alsheikhy, A.A., 2022. A fire detection algorithm using convolutional neural network. J. King Abdulaziz Univ. Eng. Sci. 32 (2).

Azari, M., Rasti, E., Dehkordi, M.H.R., Azimy, H., Zarei, A., Bagherzadeh, S.A., 2021. Investigation of temperature distribution and melt pool microstructure in laser fusion welding of Inconel 625 superalloy. J. Laser Appl. 33 (2), 022015.

Baghjari, S.H., 2013. SA Mousavi. Effects of pulsed Nd: YAG laser welding parameters and subsequent post-weld heat treatment on microstructure and hardness of AISI 420 stainless steel. Mater. Des. 43, 1–9.

Bhatt, D., Goyal, A., 2018. Effect of parameters of Nd YAG laser welding on AISI 316 Stainless steel and Brass. IOP Conf. Ser. Mater. Sci. Eng. 455, 012118, 2018/12/19.

Casalino, G., Angelastro, A., Perulli, P., Casavola, C., Moramarco, V., 2018. Study on the fiber laser/TIG weldability of AISI 304 and AISI 410 dissimilar weld. J. Manuf. Process. 35, 216–225.

Chen, Z., 2022. Research on internet security situation awareness prediction technology based on improved RBF neural network algorithm. Journal of Computational and Cognitive Engineering 1 (3), 103–108.

Chen, S., Huang, J., Xia, J., Zhao, X., Lin, S., 2015. Influence of processing parameters on the characteristics of stainless steel/copper laser welding. J. Mater. Process. Technol. 222, 43–51, 2015/08/01/.

Deng, C., Zhang, L., Deng, H., 2022. Improving sentence simplification model with ordered neurons network. CAAI Trans. Intell. Technol. 7 (2), 268–277. https://doi.org/10.1049/cit2.12047.

Ding, H., Ma, J., Zhao, C., Zhao, D., 2021. Effect of welding speed, pulse frequency, and pulse width on the weld shape and temperature distribution in dissimilar laser welding of stainless steel 308 and brass alloy. J. Laser Appl. 33 (2), 022009.

Dong, P., Xiao, R., 2009. Laser welding of lap joint between copper and brass. International Congress on Applications of Lasers & Electro-Optics 2009 (1), 203–207.

Dong, X., Hao, W., Liu, J., Wang, G., Ren, H., 2021. Effect of laser parameters on melting ratio and temperature distribution in dissimilar laser welding of brass and SS 308 using the artificial neural network model. J. Laser Appl. 33 (3), 032003.

Ducharme, R., Williams, K., Kapadia, P., Dowden, J., Steen, B., Glowacki, M., 1994. The laser welding of thin metal sheets: an integrated keyhole and weld pool model with supporting experiments. J. Phys. Appl. Phys. 27 (8), 1619.

Galun, R., Bordfeld, H., Gattermann, S., Mordike, B.L., 2002. Processing and influence on mechanical properties of precision laser beam welding of dissimilar material combination of stainless steel and brass. Laser Eng. 12 (3), 191–200, 2002/01/01.

Gaur, H., Khidhir, B., Manchiryal, R.K., 2022. Solution of structural mechanic's problems by machine learning. Int. J. Hydromechatronics 5 (1), 22–43.

Geng, Y., Akbari, M., Karimipour, A., Karimi, A., Soleimani, A., Afrand, M., 2019. Effects of the laser parameters on the mechanical properties and microstructure of weld joint in dissimilar pulsed laser welding of AISI 304 and AISI 420. Infrared Phys. Technol. 103, 103081.

Grajczak, J., et al., 2021. Influence of process-related heat accumulation of laser beam welded 1.7035 round bars on weld pool shape and weld defects. J. Laser Appl. 33 (4), 042007.

Grimvall, G., 1999. Thermophysical Properties of Materials. Elsevier.

Hanif, R., Mustafa, S., Iqbal, S., Piracha, S., 2022. A study of time series forecasting enrollments using fuzzy interval partitioning method. Journal of Computational and Cognitive Engineering. https://doi.org/10.47852/bonviewJCCE2202159.

https://www.bohlersteels.co.uk.

Huang, L., Hua, X., Wu, D., Li, F., 2018. Numerical study of keyhole instability and porosity formation mechanism in laser welding of aluminum alloy and steel. J. Mater. Process. Technol. 252, 421–431, 2018/02/01/.

Khan, M., Saeed, T., Ibrahim, M., Chu, Y.-M., Algehyne, E.A., 2021. Prediction of temperature distribution around fusion zone in fiber dissimilar laser welding of AISI 304 and AISI 420: a wavelet network nonlinear ARX model. J. Laser Appl. 33 (2), 022014, 2021/05/01.

Khan, J., Lee, E., Kim, K., 2022. A higher prediction accuracy–based alpha–beta filter algorithm using the feedforward artificial neural network. CAAI Trans. Intell. Technol 1–16. https://doi.org/10.1049/cit2.12148.

Kumar, N., Mukherjee, M., Bandyopadhyay, A., 2017. Study on laser welding of austenitic stainless steel by varying incident angle of pulsed laser beam. Opt Laser. Technol. 94, 296–309, 2017/09/01/.

Li, Y., Hu, S., Shen, J., Hu, B., 2014a. Dissimilar welding of H62 brass-316l stainless steel using continuous-wave Nd:YAG laser. Mater. Manuf. Process. 29 (8), 916–921, 2014/08/03.

Li, Y., Hu, S., Shen, J., 2014b. The effect of peak power and pulse duration for dissimilar welding of brass to stainless steel. Mater. Manuf. Process. 29 (8), 922–927, 2014/08/03.

Li, F., Wang, X., Shao, M., Wang, X., Lu, J., Liu, H., 2021. Microstructure and mechanical properties of the bonded interface of laser impact welding brass/SS304. J. Braz. Soc. Mech. Sci. Eng. 43 (4), 178, 2021/03/04.

Lin, G., Gao, S., Shi, D., 2021. Numerical investigation of temperature distribution and melt pool dimension during dissimilar laser welding of AISI 304 and pure copper. J. Laser Appl. 33 (3), 032002.

Liu, B.K., Lu, W.Z., 2022. Surrogate models in machine learning for computational stochastic multi-scale modelling in composite materials design. Int. J. Hydromechatronics 5 (4), 336–365.

Lu, J., Liu, H., Wang, K., Zhang, H., Gu, X., Wang, X., 2021. Experimental and numerical investigations on the interface characteristics of laser impact-welded Ti/brass joints. J. Mater. Eng. Perform. 30 (2), 1245–1258, 2021/02/01.

Mills, K.C., 2002. Recommended Values of Thermophysical Properties for Selected Commercial Alloys. Woodhead Publishing.

Nguyen, Q., Azadkhou, A., Akbari, M., Panjehpour, A., Karimipour, A., 2020. Experimental investigation of temperature field and fusion zone microstructure in dissimilar pulsed laser welding of austenitic stainless steel and copper. J. Manuf. Process. 56, 206–215, 2020/08/01/.

Pehlke, R.D., Jeyarajan, A., Wada, H., 1982. Summary of thermal properties for casting alloys and mold materials. NASA STI/Recon Technical Report N 83, 36293.

Peng, Y., et al., 2021. Analysis of the effect of roughness and concentration of Fe3O4/water nanofluid on the boiling heat transfer using the artificial neural network: an experimental and numerical study. Int. J. Therm. Sci. 163, 106863. /05/01/2021.

Prabakaran, M.P., Kannan, G.R., 2019. Optimization of laser welding process parameters in dissimilar joint of stainless steel AISI316/AISI1018 low carbon steel to attain the maximum level of mechanical properties through PWHT. Opt Laser. Technol. 112, 314–322, 2019/04/15/.

Saha, P., Waghmare, D., 2020. Parametric optimization for autogenous butt laser welding of sub-millimeter thick SS 316 sheets using central composite design. Opt Laser. Technol. 122, 105833, 2020/02/01/.

Sasaki, M., Ikeno, J., 2011. Laser butt welding of brass and stainless steel. Journal of Advanced Mechanical Design, Systems, and Manufacturing 5 (4), 347–357.

Wang, L., Rong, Y., 2022. Review on processing stability, weld defects, finite element analysis, and field assisted welding of ultra-high-power laser (≥ 10 kW) welding. Int. J. Hydromechatronics 5 (No. 2), 167–190.

Wang, J., Sun, Z., Gu, L., Azimy, H., 2021. Investigating the effect of laser cutting parameters on the cut quality of Inconel 625 using Response Surface Method (RSM). Infrared Phys. Technol. 118, 103866, 2021/11/01/.

Xia, P., Yan, F., Kong, F., Wang, C., Liu, J., Hu, X., Pang, S., 2014. Prediction of weld shape for fiber laser keyhole welding based on finite element analysis. Int. J. Adv. Des. Manuf. Technol. 75 (1–4), 363–372.

Yang, H., et al., 2021. Study on laser welding of copper material by hybrid light source of blue diode laser and fiber laser. J. Laser Appl. 33 (3), 032018.

Yongbin, Y., Bagherzadeh, S.A., Azimy, H., Akbari, M., Karimipour, A., 2020. Comparison of the artificial neural network model prediction and the experimental results for cutting region temperature and surface roughness in laser cutting of AL6061T6 alloy. Infrared Phys. Technol. 108, 103364, 2020/08/01/.

Yu, D., Liao, Q., Zhang, B., Ghaderi, M., 2021. Pulsed laser welding and microstructure characterization of dissimilar brass alloy and stainless steel 308 joints. J. Laser Appl. 33 (2), 022017.

Zhang, Z., Farahmand, P., Kovacevic, R., 2016. Laser cladding of 420 stainless steel with molybdenum on mild steel A36 by a high power direct diode laser. Mater. Des. 109, 686–699.

Zhang, J., et al., 2021. Laser pressure welding of copper. Opt Laser. Technol. 134, 106645, 2021/02/01/.